Monthly Notices
of the
ROYAL ASTRONOMICAL SOCIETY

MNRAS **490,** 3098–3111 (2019)
Advance Access publication 2019 October 3

doi:10.1093/mnras/stz2738

The thermal-radiative wind in low-mass X-ray binary H1743−322: radiation hydrodynamic simulations

Ryota Tomaru,[1,2]★ Chris Done,[2,3] Ken Ohsuga,[4] Mariko Nomura[5] and Tadayuki Takahashi[1,2]

[1]*Department of Physics, The University of Tokyo, 7-3-1 Hongo, Bunkyo, Tokyo 113-0033, Japan*
[2]*Kavli Institute for the Physics and Mathematics of the Universe (WPI), University of Tokyo, Kashiwa 277-8583, Japan*
[3]*Centre for Extragalactic Astronomy, Department of Physics, University of Durham, South Road, Durham DH1 3LE, UK*
[4]*Center for Computational Sciences, University of Tsukuba, 1-1-1 Ten-nodai, Tsukuba, Ibaraki 305-8577, Japan*
[5]*Faculty of Natural Sciences, National Institute of Technology, Kure College, 2-2-11 Agaminami, Kure, Hiroshima 737-8506, Japan*

Accepted 2019 August 4. Received 2019 July 30; in original form 2019 May 28

ABSTRACT

Blueshifted absorption lines are seen in high inclination black hole binary systems in their disc-dominated states, showing these power an equatorial disc wind. While some contribution from magnetic winds remain a possibility, thermal and thermal-radiative winds are expected to be present. We show results from radiation hydrodynamic simulations that show that the additional radiation force from atomic features (bound–free and lines) is important along with electron scattering. Together, these increase the wind velocity at high inclinations, so that they quantitatively match the observations in H1743−322, unlike purely thermal winds that are too slow. We highlight the role played by shadowing of the outer disc from the (subgrid) inner disc Compton heated layer, and show that the increase in shadow from the higher Compton temperature after the spectral transition to the hard state leads to strong suppression of the wind. Thermal-radiative winds explain all of the spectral features (and their disappearance) in this simplest wind system and magnetic winds play only a minor role. We speculate that thermal-radiative winds can explain all the spectral features seen in the more complex (larger disc size) binaries, GRO J1655−40 and GRS 1915+105, without requiring magnetic winds.

Key words: accretion, accretion discs – black hole physics – hydrodynamics – X-rays: binaries.

1 INTRODUCTION

Outflowing gas is ubiquitous in accreting systems across mass scale from protostars (e.g. Bachiller 1996; Carrasco-González et al. 2010) through to both stellar mass compact objects in X-ray binaries (e.g. Remillard & McClintock 2006; Díaz Trigo & Boirin 2016) and supermassive black holes in active galactic nuclei (AGN) at the centre of galaxies (e.g. Heckman, Armus & Miley 1990; Hagino et al. 2016). These outflows, as either highly collimated jets (e.g. Burrows et al. 1996; Mirabel & Rodríguez 1999; Remillard & McClintock 2006) or wider angle winds (e.g. Ueda, Yamaoka & Remillard 2009; Tombesi et al. 2010), can have a large mass and/or kinetic power so they can have a significant impact on the accretion environment. The important open questions in the field are how these outflows are driven, whether there are common processes across these very different objects, and whether there is a causal relation between jets and disc winds. Here we address these questions in the specific setting of the Galactic compact objects.

Low-mass X-ray binary systems, both neutron star binaries (NSBs) and black hole binaries (BHBs) can show blueshifted absorption lines from highly ionized ions. These winds are fairly slow, typically less than 1000 km s^{-1} (Miller et al. 2015), seen preferentially in high inclination systems (e.g. the compilation by Ponti et al. 2012) where the binary separation is large (e.g. Díaz Trigo & Boirin 2016). These features indicate an equatorial disc wind launched from large radii, where the latter is indicated both by the wind preference for large systems and its slow velocity. The final observational constraint is that the winds are seen only when the spectra are soft and fairly luminous, in disc-dominated states, rather than in the Compton-dominated hard state (Ponti et al. 2012; Ponti, Muñoz-Darias & Fender 2014). The spectral change can be explained as a transition between a disc and hot accretion flow, where the collapse of the larger scale height hot flow into a geometrically thin disc also triggers the collapse of the steady compact radio jet (see e.g. the review by Done, Gierliński & Kubota 2007). This association of the onset of the wind with the suppression

★ E-mail: ryota.tomaru@ipmu.jp

of the jet was first noted in GRS 1915+105 by Neilsen & Lee (2009), who suggested that the same magnetic field responsible for the jet in the hard state underwent a reconfiguration to power a wind by Lorentz force (magnetic wind) in the soft state. This is consistent with the general disappearance of the wind in the hard states (see e.g. Ponti et al. 2012), though not with the simultaneous observation of jets and winds in more complex intermediate states (e.g. Homan et al. 2016; Kalemci et al. 2016), nor does it explain the preference of winds for systems with larger discs. Also, the current magnetic wind models (Fukumura et al. 2010) require a special configuration of the large-scale magnetic fields threading accretion disc, but the existence of such magnetic fields is unknown.

Instead, thermal winds have a clear link to both disc size and illuminating spectrum and luminosity. The pioneering work by Begelman, McKee & Shields (1983, hereafter B83) showed that bright X-ray emission from the inner disc and corona heats the surface of the disc at larger radii to the Compton temperature, $T_{\rm IC}$. This temperature depends only on the spectrum of the radiation, so the entire disc surface has a heated atmosphere at this temperature, which is unbound at radii $R_{\rm IC}$ where this temperature means that particles have enough energy to escape, i.e. $kT_{\rm IC} = GM_{\rm c}\mu m_{\rm p}/R_{\rm IC}$, where μ is the mean molecular weight, set to 0.61. This launches a thermal wind at radii larger than the inverse Compton radius, $R_{\rm IC} \sim (6.4 \times 10^4/T_{\rm IC,8})R_{\rm g}$ ($R_{\rm g} = GM_{\rm c}/c^2$, $T_{\rm IC,8} = T_{\rm IC}/10^8$ K), giving a clear dependence on both the spectrum (through $T_{\rm IC}$) and the disc size, as observed.

However, such thermal wind solutions were disfavoured due to a single, highly anomalous, wind from GRO J1655−40, where the wind launch radius could be inferred from density diagnostics. The observed ionization state was unusually low for these winds, at $\xi = L/nR^2 \sim 100$, while the density measured from metastable levels was quite high. The observed luminosity was fairly low, so the derived launch radius was much smaller than $R_{\rm IC}$, ruling out a thermal wind (Miller et al. 2006a; Kallman et al. 2009; Luketic et al. 2010; Neilsen & Homan 2012; Higginbottom & Proga 2015). However, the unusual properties of the broad-band continuum seen during this observation indicate that the intrinsic source luminosity may be substantially underestimated, with the wind being so strong that it has become optically thick (Done, Gierliński & Kubota 2007; Uttley & Klein-Wolt 2015; Neilsen et al. 2016; Shidatsu, Done & Ueda 2016).

Done, Tomaru & Takahashi (2018, hereafter D18) revisited the thermal wind models of B83, combining their analytic equations for the mass-loss rate with the hydrodynamic results of Woods et al. (1996) to predict the wind observables of column density, ionization state, and velocity as a function of spectral shape, luminosity, and inclination. They stressed that the observed winds are generally seen at fairly high $L/L_{\rm Edd}$, and suggested that radiation force could play an important role, so that the winds are more accurately described as thermal-radiative rather than simply thermal.

Here we show the first hydrodynamic simulations of thermal-radiative winds with realistic illuminating spectra and full opacities. We tailor these simulations for the typical BHB system H1743−322, where *Chandra* grating data clearly detect the wind during a soft state, but show only tight upper limits on similar absorption features during a hard state. We show that the wind velocity in the soft state is much faster than predicted by purely thermal winds (see also Luketic et al. 2010; Higginbottom & Proga 2015), but that the radiation force from the combination of electron scattering and atomic opacities (both edges and lines) produces additional driving that increases the wind velocity at high inclinations, matching well to that observed. We show that the strong suppression of the wind when the system switches to the hard state is predicted by the thermal-radiative wind models as claimed in D18, but for a rather different reason, more connected to radiation transfer effects in the inner disc atmosphere than to the different outer disc wind properties. These simulations demonstrate that thermal-radiative winds are the origin of most (perhaps all) of the outflows seen in Galactic compact binaries.

2 THE BHB H1743−322

There are currently four BHBs that show wind features in their soft states, namely GRO J1655−40, GRS 1915+105, H1743−322, and 4U 1630−472 (see e.g. the compilation of Ponti et al. 2012). The anomalous features of the wind in one observation of GRO J1655−40 are discussed above (though see Higginbottom et al. 2018) for a thermal wind simulation of a more normal soft state. GRS 1915+105 has a mean luminosity around Eddington, so radiation force will be extremely important. It also typically shows complex spectra rather than standard soft or hard states, and has a truly enormous disc so needs a very large simulation domain. The system parameters for 4U 1630−472 are not well known and it has a very large galactic column that makes determining the soft state disc luminosity difficult.

This leaves H1743−322 as the best object to model in detail. This object has recurrent transient outbursts, switching from hard to soft on the fast rise, and soft to hard on the slower decline. *Chandra* High Energy Transmission Grating (HETG) observations during a standard disc-dominated state in 2003 show blueshifted absorption lines from Fe XXV and Fe XXVI (ObsID: 3803; see Miller et al. 2006b), with only upper limits on these absorption lines in the hard state in 2010 (ObsID: 11048; see Miller et al. 2012). We reanalyse the data of soft state, and fit with Gaussian absorption line (GABS in XSPEC) to get columns and velocity. We find these values are within $\pm1\sigma$ errors of those of previously reported, i.e. the column and velocity of Fe XXV, $N_{\rm XXV} = 8.2^{+1.2}_{-1.1} \times 10^{16}$ cm^{-2} and $V_{\rm XXV} = 370 \pm 120$ cm^{-2}, while those of Fe XXVI are $N_{\rm XXVI} = 4.0 \pm 0.3 \times 10^{17}$ cm^{-2} and $V_{\rm XXVI} = 630^{+80}_{-120}$ km s^{-1}.

We adopt system values from Shidatsu & Done (2019), where $M = 7$ M$_\odot$, $D = 8.5$ kpc, and inclination of $75^\circ \pm 3^\circ$ (Steiner, McClintock & Reid 2012). We note that these are different to those assumed in D18, so that the observed bolometric luminosities from the *RXTE* Proportional Counter Array (PCA) data for the soft and hard state correspond to $L/L_{\rm Edd} = 0.3$ and 0.06 (compare to 0.1 and 0.02 in D18).

The remaining key parameter that determines the strength of a thermal wind is the disc size, $R_{\rm disc}$. This is quite poorly known. D18 assume $R_{\rm disc} = 5R_{\rm IC}$ to connect to the hydrodynamic simulations of Woods et al. (1996) but Shidatsu & Done (2019) note that the outburst frequency puts the source on the edge of the disc instability, similarly to GX 339-4. We use the Monitor of all-sky X-ray Image (MAXI) light curve to measure the mean X-ray luminosity over a 10-yr time span. The mean MAXI 2–20 keV count rate is about 10 times lower than the count rate seen during the low/hard state ($L/L_{\rm Edd} = 0.06$) used by Shidatsu & Done (2019). This converts to a mean mass transfer rate of $\sim 6 \times 10^{16}$ g s^{-1}, where the disc instability condition predicts an orbital period of $\sim$7 h (Coriat, Fender & Dubus 2012). Assuming the companion star has a similar mass ratio as in GX 339-4, then this implies a Roche lobe size of 1.7×10^{11} cm, and hence a disc radius of 1.2×10^{11} cm (70 per cent Roche lobe size), which is $0.2R_{\rm IC}$. This is the point at which thermal winds are launched, so the wind will depend quite sensitively on size scale here. Given the uncertainties, we start first by calculating the wind produced by a disc with $R_{\rm disc} = R_{\rm IC}$, and then explore the effect of changing parameters.

3 COMPUTATIONAL METHOD

3.1 Code overview

Our radiation-hydrodynamic simulation code was developed by Takahashi & Ohsuga (2013), described most recently in Nomura et al. (2016). This is similar to the code used in earlier work by Proga, Stone & Kallman (2000) and Proga & Kallman (2004). We solve the standard equations of motion in spherical polar coordinates, including the radiation force on the material, together with the continuity equations for mass and energy equation, where the latter includes a net heating/cooling term for the material, $\mathcal{L}$. This is defined by

$$\rho\mathcal{L} = \left(\frac{\rho}{\mu m_{\rm p}}\right)^2 [\Gamma(\xi, T) - \Lambda(\xi, T)], \quad (1)$$

where mass density and number density are related by $\rho = n\mu m_{\rm p}$. The heating, Γ, and cooling, Λ, rates per unit volume are calculated by CLOUDY (Ferland 2003), although the simple heating and cooling functions are employed in Nomura et al. (2016). These depend on the shape of the illuminating spectrum, which is discussed in more detail in the next section, as well as on the temperature T and ionization parameter:

$$\xi(R, \theta) = \frac{L_{\rm x}}{nR^2} = \frac{4\pi\mu m_{\rm p} F_{\rm x}}{\rho}, \quad (2)$$

where $F_{\rm x}$ is the X-ray flux and $L_{\rm x}$ is the X-ray luminosity at each grid point. These are defined from the intrinsic luminosity, $L_{\rm x0}$, which is modified for absorption/scattering along the line of sight so that $L_{\rm x} = L_{\rm x0}\, {\rm e}^{-\tau(R,\theta)}$. We assume that the corona and inner disc are both effectively a central point source, so that

$$\tau(R, \theta) = \sum M(\xi, T)\kappa_{\rm es}\rho(R, \theta)\delta R + \tau_0(\theta), \quad (3)$$

where $\kappa_{\rm es} = 0.34$ cm^2 g^{-1} is the mass-scattering coefficient for free electrons, τ_0 is optical depth of inner corona described in Section 3.3, and $M(\xi, T)$ is the force multiplier defined by Tarter & McKee (1973). This force is calculated by CLOUDY and accounts for the additional opacity from continuum process (bound–free; photoelectric absorption edges) and line process (bound–bound transitions; Fig. 2b), but does not include the additional force from velocity shifts as the velocity is low. This also defines the radiation force on the material as $f_{\rm rad} = \frac{\kappa_{\rm es} M(\xi,T)}{c} F_{\rm x}$ [cm s^{-2}]. CLOUDY also calculates the ion fractions of Fe XXV and Fe XXVI, $f_{\rm XXV}(\xi, T)$ and $f_{\rm XXVI}(\xi, T)$ at each point of ξ and T.

We adopt an irradiated disc shape, where $H_{\rm d}/R \propto R^{2/7}$ (Cunningham 1976, as recast by Kimura & Done 2019) where

$$H_{\rm d}/R = 1.5\times10^{-3}\left(\frac{L}{L_{\rm Edd}}\right)^{1/7}\left(\frac{M_{\rm c}}{{\rm M}_\odot}\right)^{-1/7}\left(\frac{R_{\rm out}}{R_{\rm g}}\right)^{2/7}\left(\frac{R}{R_{\rm out}}\right)^{2/7}$$
$$= f_{\rm d}\left(\frac{R}{R_{\rm out}}\right)^{2/7}. \quad (4)$$

In the simulation grid, we set angle of disc from mid-plane $\alpha_{\rm d}(R) = \arctan\{H_{\rm d}(R)/R - H_{\rm d}(R_{\rm in})/R_{\rm in}\}$ in order to set $\alpha_{\rm d} = 0$ ($\theta = \pi/2$) at inner radius of computational domain $R_{\rm in}$ (see also Appendix A).

We apply the axially symmetric boundary at the rotational axis of the accretion disc, $\theta = 0$ so that ρ, p, and v_r are symmetric, while v_θ and v_ϕ are antisymmetric). We apply a reflecting boundary at $\theta = \pi/2$ so that ρ, p, v_r, and v_ϕ are symmetric, but v_θ is antisymmetric. Outflow boundary conditions are employed at the inner and outer radial boundaries, so that matter can freely leave but not enter the computational domain. We set our radial computational grid from $R = (0.01 - 1)R_{\rm out}$, with 120 values logarithmically spaced. Our assumed value of $R_{\rm out} = 6.6\times10^5 R_{\rm g}$ is coincidentally equal to $R_{\rm IC}$ for the Compton temperature of the soft state spectral energy distribution (SED) of 1.0×10^7 K.

We set a specific polar angle grid to follow the shape of the disc surface, so we take 120 values of θ to cover the disc/atmosphere transition for angles $\theta > \pi/2 - \alpha_{\rm d}(R_{\rm out})$ and another 120 values to cover the wind region with constant solid angle $\mathrm{d}(\cos\theta) = \sin\theta\,\mathrm{d}\theta$. In the disc zone and disc surface, we set $v_R = 0$, $v_\phi = v_k = \sqrt{GM_{\rm c}/R}\sin\theta$ at each time step.

We initially set temperature $T(R, \theta) = 1.1\times10^7(R/6R_{\rm g})^{-3/4}$ K, density $\rho_0(R, \theta) = 1.0\times10^{-33}$ g cm^{-3} (except in the disc region), $v_R(R, \theta) = 0$, $v_\theta(R, \theta) = \sqrt{GM/R}\sin\theta$, and $v_\phi(R, \theta) = 0$.

For comparison with observation, we calculate the ion density of Fe XXVI and Fe XXV from simulations via $n_{\rm XXVI} = n\, A_{\rm Fe} f_{\rm XXVI}(\xi, T)$ and $n_{\rm XXV} = n\, A_{\rm Fe} f_{\rm XXVI}(\xi, T)$, where $A_{\rm Fe} = 3.3\times10^{-5}$ is iron abundance relative to hydrogen that is the same value as Miller et al. (2006b). We use these to define the ion column density along any line of sight, and to calculate the column density weighted mean velocity for each ion.

3.2 Ionization state calculations

We focus first on the soft state, where the absorption lines are detected, and show the SED from quasi-simultaneous *RXTE* PCA data (ObsIDs P95368-01-01-00) in Fig. 1(a). We use this to calculate the heating and cooling rates from CLOUDY, assuming that the illuminated gas is optically thin. Fig. 1(b) shows the heating and cooling rates for material at a given temperature and pressure ionization parameter $\Xi = P_{\rm rad}/P_{\rm gas} = L/(4\pi R^2 cnkT) = (\xi/T)\times 1/(4\pi ck)$, where ξ is the standard ionization parameter defined above. Thermal equilibrium is produced when the heating rate per unit volume is equal to its cooling rate, as indicated by the heavy black line in Fig. 1(b). The blue region to the left of this curve shows that the cooling rates are larger than the heating rates, whereas the opposite orange region shows that the heating rates are larger rate than cooling rates. The solutions with positive slope, i.e. $\mathrm{d}T/\mathrm{d}\Xi > 0$ are thermally stable because if the temperature rises slightly from this curve fixing Ξ, the cooling rates are larger than the heating rates and the temperature goes down. For the opposite reason, those with negative slope are thermally unstable. The changing points of the sign of slope are instability points.

This thermal equilibrium curve has a very complex shape, with four stable branches separated by regions of instability and/or rapid change (Fig. 1b, with zoom in Fig. 1c). This is very different to the single S-shaped thermal equilibrium curve using in B83, where there is a minimum pressure ionization parameter associated with the material on the hot branch, $\Xi_{\rm h,min}$ at the temperature $\sim\frac{1}{2}T_{\rm IC}$ that marks the bottom of the heated atmosphere, while the maximum pressure ionization parameter associated with material on the cold branch $\Xi_{\rm c,min}$, marks the top of the disc. Instead, for this more complex shape, we take the minimum pressure ionization parameter of the long middle branch (associated with partially ionized oxygen and iron L shell) to mark the bottom of the heated atmosphere, i.e. we set $\Xi_{\rm H,min} = \Xi_{\rm m,min} = 8.2$, where $T \ll T_{\rm IC}$.

Fig. 2(a) shows this equilibrium curve in the standard ionization parameter representation. The $\Xi_{\rm m,min}$ point corresponds to material with $\xi = 170$, where the soft X-ray opacity is already substantial. The maximum pressure ionization parameter on the cold branch, $\Xi_{\rm c,max} \sim 7.4$, has standard $\xi \sim 14$ (see Fig. 2a), so it is underneath layers with $14 \le \xi \le 170$. This material has very substantial opacity so it seems very unlikely that it can be irradiated directly by the

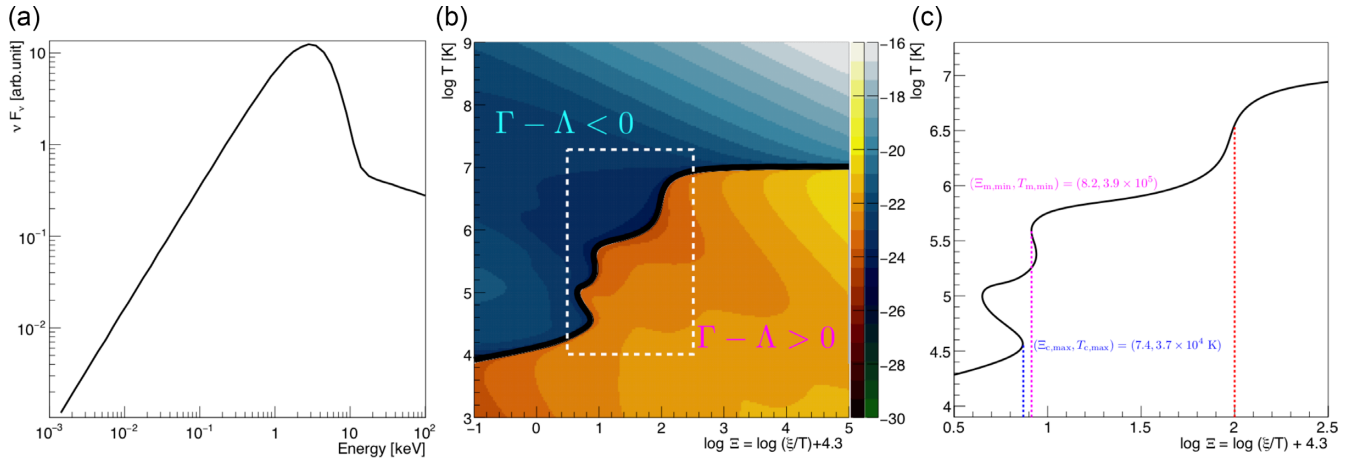

Figure 1. (a) The energy flux of H1743−322 that consists of a disc blackbody plus Comptonized power law (DISKBB+DISKBB*SIMPLE in XSPEC). (b) The heating and cooling function ($\Gamma - \Lambda$). The black curve shows the thermal equilibrium ($\Gamma - \Lambda = 0$), the right-hand colour bar shows the absolute logarithm value of heating minus cooling function ($\log|\Gamma - \Lambda|$). The Compton temperature of this spectrum is $T_{\rm IC} = 1.0 \times 10^7$ K. (c) The zooming figure of (b) surrounding by white dashed line. The vertical lines show the instability points. Red vertical lines are $\Xi_{\rm h,min} = 100$.

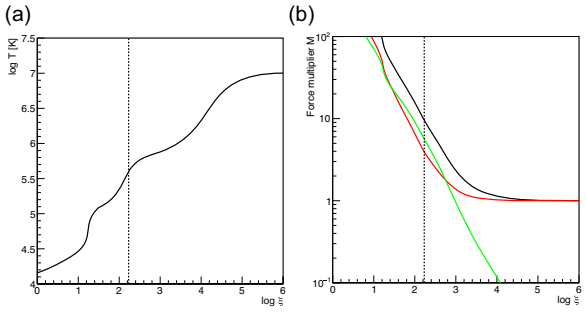

Figure 2. (a) Thermal equilibrium curve of $\log \xi$ versus $\log T$. (b) Force multiplier of continuum process (bound–free plus scattering, red), line (green) and total (black) at the thermal equilibrium state. The vertical dashed line shows $\xi_{\rm H,min} = 1.7 \times 10^2$ that is the ionization parameter of disc surface.

source SED. Hence we assume the disc surface also has $\Xi_{\rm m,min}$, i.e. we set $\Xi_{\rm C,max} = \Xi_{\rm m,min}$. These are almost identical in Ξ (see Fig. 1c), but quite different in ξ due to their very different temperatures. We use thermal equilibrium to set density at the disc surface to $\xi = 170$. At each time step, the density of disc surface is update via $n = L_{\rm x}/(170R^2)$ and check that temperature is hotter than that of the viscous heated disc across the entire grid.

3.3 Inner attenuating corona

The original thermal wind paper of B83 gives an overview of the structure of the Compton heated upper layers of the disc for optically thin material. In this limit, the heated material above the inner disc forms a static atmosphere with scale height $H_{\rm c}/R \sim (v_{\rm IC}/v_{\rm g}) = (T_{\rm IC}/T_{\rm g})^{1/2}$, where $v_{\rm g}$ ($T_{\rm g}$) is the escape velocity (virial temperature). This gives $H_{\rm c} \sim [2R^3/R_{\rm IC}]^{1/2}$. However, Begelman & McKee (1983, hereafter BM83) show that it is easy for this heated atmosphere to go optically thick in the radial direction along the disc plane, so it forms an inner attenuation zone, reaching $\tau = 1$ at $R_{\rm ia}$ given by

$$\frac{R_{\rm ia}}{R_{\rm IC}} = 0.021 \left[\frac{T_{\rm IC,8}(L/L_{\rm Edd})}{\Xi_{\rm H,min}} \right]^{1/2}. \quad (5)$$

For our soft state simulation this gives $R_{\rm ia} \sim 0.0004 R_{\rm IC} \sim 200 R_{\rm g}$. This radius is on scales that are more than an order of magnitude

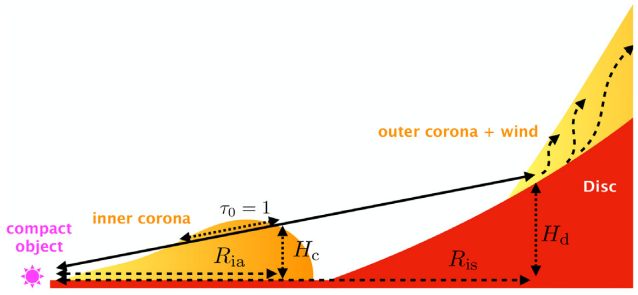

Figure 3. Schematic view of an inner corona and a wind.

smaller than the starting point of our radial grid, so this structure cannot be resolved by our simulation. However, it strongly affects the wind properties in the simulation range as it casts a shadow over the disc surface out to large radii (see Fig. 3). The outer disc is only directly irradiated again when the disc scale height increases by a large enough factor that it rises above the shadow zone. For an irradiated disc with scale height given by equation (4), then the shadow cast by the inner attenuation zone ends at $R_{\rm is}$, where the disc is directly illuminated again. The geometry gives $H_{\rm d}/R_{\rm is} = H_{\rm c}/R_{\rm ia}$ so that

$$R_{\rm is} = 3.0 \times 10^7 \, T_{\rm IC,8}^{7/8} \left(\frac{M_{\rm c}}{{\rm M}_\odot} \right)^{1/2} \left(\frac{L}{L_{\rm Edd}} \right)^{3/8} \Xi_{\rm h,min}^{-7/8} R_{\rm g}. \quad (6)$$

This gives $R_{\rm is} = 0.18 R_{\rm IC}$ for $L/L_{\rm Edd} = 0.3$ for our assumed system parameters with the soft state SED. We incorporate the subgrid physics of this inner attenuating corona by changing the illumination pattern on to the disc in the outer regions that are covered by the hydrodynamic grid. We define a critical angle from the mid-plane $\alpha_{\rm c} = H_{\rm c}/R_{\rm ia}$ and assume that the optical depth from the centre to any point on the disc surface has $\tau = \exp[1 - (\alpha/\alpha_{\rm c})^2]$ and use this to attenuate the X-ray luminosity by $e^{-\tau}$ before it enters the grid.

4 RESULTS FOR FIDUCIAL SOFT STATE SPECTRAL ENERGY DISTRIBUTION

We run a series of simulations as described below, with parameters and resulting mass-loss rates given in Table 1. All simulations run

Table 1. The summary of simulations and inner corona parameters.

SED[a]	$L/L_{\rm Edd}$	$F_{\rm rad}$	$T_{\rm IC}$ (10^8 K)	$R_{\rm IC}/R_{\rm out}$	$H_{\rm out}/R_{\rm out}$	$\Xi_{\rm h,min}$	$R_{\rm ia}$ ($R_{\rm g}$)	$H_{\rm c}$ ($R_{\rm g}$)	$R_{\rm is}/R_{\rm out}$	$R_{\rm disc}/R_{\rm out}$	$\dot{M}_{\rm w}$ (10^{18} g s^{-1})	$\dot{M}_{\rm w}/\dot{M}_{\rm a}^{b}$
S	0.3	Y	0.10	1	0.044	100	240	6.4	0.18	1.0	21	6.0
S	0.3	N	0.10	1	0.044	100	240	6.4	0.18	1.0	8.7	2.5
S	0.3	Y	0.10	1	0.044	100	240	6.4	0.18	0.18	1.2	0.34
S	0.5	Y	0.10	1	0.047	100	310	9.5	0.22	1.0	28	4.8
S	0.5	N	0.10	1	0.047	100	310	9.5	0.22	1.0	14	2.4
S	0.1	Y	0.10	1	0.038	100	140	2.8	0.12	1.0	1.8	1.5
S	0.3	Y	0.10	1	0.044	–	640	28	1.0	1.0	5.6	1.6
S	0.5	Y	0.10	1	0.047	–	730	34	1.0	1.0	7.9	1.3
H	0.06	N	0.70	0.14	0.035	3.3	220	22	11	1.0	0.43	0.61

[a]S: soft state; H: hard state.
[b]$\dot{M}_{\rm a} = L/(0.1c^2)$.

for 9 sounds crossing time ($c_{\rm IC}/R_{\rm IC} = \sqrt{kT_{\rm IC}/(\mu m_{\rm p})}/R_{\rm IC}$). This corresponds to 1.7×10^5 s.

4.1 Fiducial simulation: effect of radiation force

We first run a fiducial simulation, for the soft state SED in Fig. 1, assuming $L/L_{\rm Edd} = 0.3$. We include all radiation force terms (electron scattering, bound–free, and line), attenuation of these effects, and fiducial inner corona defined by equation (3). The derived density and temperature structure are shown in Appendix B (top left in Fig. B1) and the total mass-loss rate through the outer boundary is 21×10^{18} g s^{-1} (see Table 1). The black lines in Fig. 4 show the column density (upper panel) and velocity (lower panel) as a function of inclination angle for this simulation, with Fe XXVI as the solid line and Fe XXV as dashed.

We compare this to the results from a simulation where we turn-off all the radiation force terms and their attenuation except inner corona ($M = 0$ in equation 3), so that the wind only is thermally driven (top middle in Fig. B1 and red lines in Fig. 4). This simulation has much lower total mass-loss rate, of 8.7×10^{18} g s^{-1}, so it is clear that radiation force is important, and that this wind is better described as thermal-radiative rather than simply thermal. The thermal wind has a very low velocity at high inclination angles, close to the equatorial plane of the disc, so it has very large column density in these directions. Neither of these matches well to the observations at the inferred high inclination angle of H1743−322 (shown by the cyan points).

Including the full radiation force terms gives a dramatic increase in velocity at large inclination angles. This is because this material close to the disc is mainly on the middle branch of the thermal equilibrium curve, i.e. at an ionization parameter close to $\xi \sim 170$, with the corresponding temperature that is substantially less than the Compton temperature, so the material forms a mainly static atmosphere rather than an outflowing corona (Higginbottom & Proga 2015; Higginbottom et al. 2018). The presence of the middle branch of the S curve for this soft continuum spectrum gives the difference between these calculations and the earlier exploration of Proga & Kallman (2002), where they showed that the radiative force was negligible for a much harder continuum.

Instead, when radiation force is included, this warm, partially ionized material has enough opacity for bound–free and bound–bound opacity to accelerate it out so it can escape as a wind. This increases in velocity more than offsets the increased amount of material that escapes, so the column density decreases.

We investigate which term of the radiation force is most important at any ξ. Fig. 2(b) shows force multiplier of the continuum process (red), lines process (green), and their sum (black) at thermal equilibrium state. Radiation force on free elections may have some impact on the simulations, but at our luminosity of only $0.3L_{\rm Edd}$, this alone is not enough to unbind much material. We run an additional simulation including only this term, and find a total mass-loss rate of 8×10^{18} g s^{-1}, so same within 10 per cent than the purely thermal wind. Fig. 2(b) shows that the radiation force on lines and photoelectric opacities have similar magnitudes, and that adding all the terms together gives a force multiplier of around $M = 9.6$ at $\xi = 170$, thus the ratio of total radiation force to gravity is $M \times L/L_{\rm Edd} = 0.3 \times 9.6 > 1$. Neglecting line opacity but including electron scattering and bound–free gives a force multiplier of 3.6, so this is just enough to get to unbind the material when it is launched, but not enough to continue accelerating it once it becomes more ionized. We rerun a simulation including only electron scattering and bound–free opacities and find a mass-loss rate of 9.8×10^{18} g s^{-1}. Thus it is the combination of all opacity sources that is important at high but subcritical $L/L_{\rm Edd}$ values, and a single correction factor for $L/L_{\rm Edd}$ (as in D18) is too simplistic to describe the behaviour revealed.

4.2 Changing the disc size

Thermal winds depend most sensitively on the shape of the spectrum, the luminosity, and the size of the disc. The spectral shape is defined by observations, but the overall luminosity and disc size depend on the assumed system parameters that are poorly known. The analytic models give a dependence on $N_{\rm H} \propto \log R_{\rm disc}/R_{\rm in}$, where $R_{\rm in} = 0.2R_{\rm IC}$ is the launch radius of the wind. However, the reduction in column required from the data is not simple to produce in the analytic approximation of D18 as Fe XXVI should decrease by factor of 5 but that of Fe XXV should decrease by 2 orders magnitude at 75°. However, we note that our disc size is already only $R_{\rm disc} = R_{\rm IC}$, and the analytic approximations probably become unreliable as we approach the wind launch radius.

Instead, we reduce the disc size to $R_{\rm disc} = 0.18R_{\rm out}$, which is the same radius as inner shadow radius and the wind launch radius, then we rerun the simulation including full radiation force. We run the simulation over the same grid as before, but set a very low density at mid-plain ($\theta = 90°$) when the radius is larger than the disc radius. The blue line in Fig. 5 shows the results of this simulation. We can reproduce the ion columns seen in the data, and in particular we now have a higher column of Fe XXVI than Fe XXV, indicating a higher ionization state for the wind. The wind is launched, but only just! The mass-loss rate is 20 times smaller than that of fiducial simulation, so the density of the wind is quite low. It is still slightly overshadowed, so the disc is not fully illuminated by the central source, but the drop in overall mass accretion rate

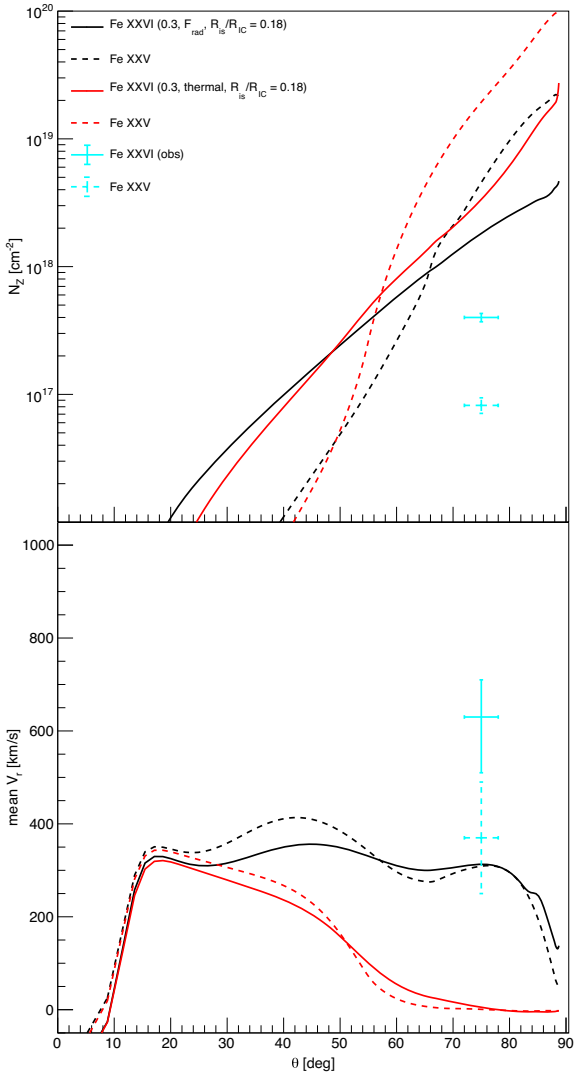

Figure 4. Top: the inclination dependence of column densities of Fe XXVI (solid line) and Fe XXV (dashed line). Bottom: the inclination dependence of column weighted mean velocities of Fe XXVI (solid line) and Fe XXV (dashed line). The colours show the thermal-radiative wind of $L/L_{\rm Edd}$ = 0.3, $R_{\rm IS}/R_{\rm IC} = 0.18$ (black), and the thermal wind (red).

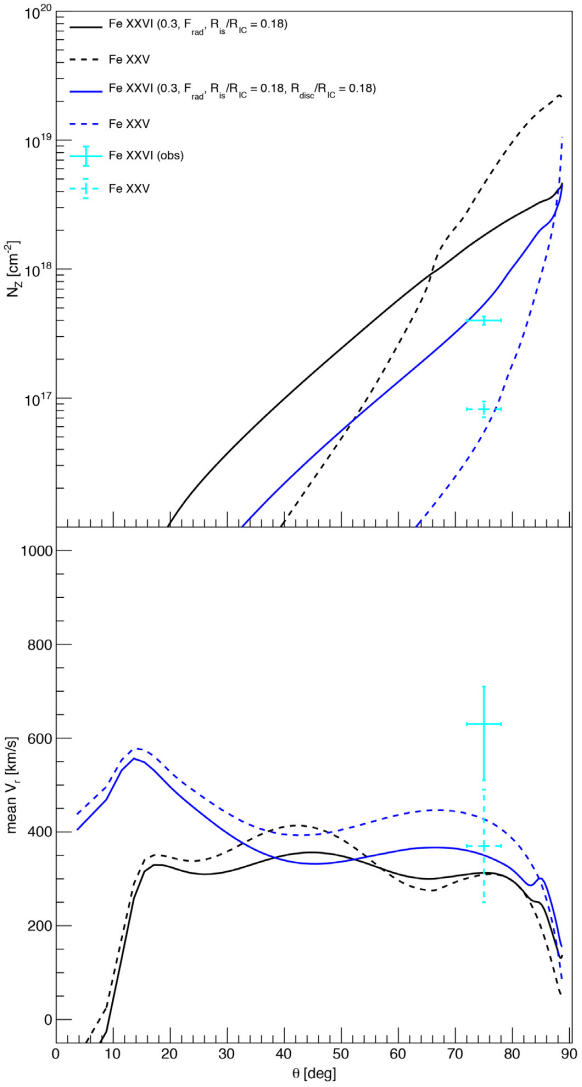

Figure 5. As in Fig. 4, but for $R_{\rm disc}/R_{\rm IC}$ = 1.0 (black) and 0.18 (blue).

reduces the density sufficiently for the ionization parameter to be higher than before. This means that the contribution of line and photoelectric absorption to the driving is almost negligible. This wind is driven by the combination of radiation force on electrons and gas pressure gradient force, and its velocity matches well to that measured in the data.

We explore the effect of some of the other parameters input into the fiducial simulation below in order to illustrate their impact on the predicted wind, but this is our best match overall to the observed data.

4.3 Changing luminosity: $L/L_{\rm Edd} = 0.5$ and 0.1

We now consider the effect of changing luminosity. We run an additional set of simulations with $L/L_{\rm Edd} = 0.5$ for the same SED. This changes the radius of inner attenuation zone and the outer disc scale height, so that the shadow extends to $R_{\rm is} = 0.22R_{\rm out}$. Fig. 6 shows the resultant column density (upper) and velocity (lower) for this simulation including all radiation forces (green) compared to a purely thermal wind at the same luminosity (yellow). The purely thermal results are very similar to those at $L/L_{\rm Edd} = 0.3$, with very low velocity at high inclination angles, and consequently large column density. This material is again mainly on the middle branch of the ionization instability, so it does not have high enough temperature to escape. However, including radiation force on this material makes even more difference at these higher luminosities, so the column is lower and the velocity higher than for $L/L_{\rm Edd} = 0.3$, bringing the models closer to the observed data points (cyan).

We also run a simulation including all radiation force terms with the same SED but $L/L_{\rm Edd} = 0.1$. Fig. 7 shows the column and velocity from this (violet) compared to $L/L_{\rm Edd} = 0.3$ (black) and 0.5 (green) including all radiation force terms. The column densities in each ion are remarkably similar, but the velocity increases dramatically at high inclination angles, and the total mass-loss rate increases from 1.8 to 21 to 28 $\times$ 10^{18} g s^{-1}.

Fig. 7 clearly shows that thermal-radiative winds are fast enough to match the observations for $L/L_{\rm Edd} \gtrsim 0.3$, but that these luminosities give columns that are a factor of 3–10 larger than the observed. There are multiple ways we can reduce the wind efficiency. As

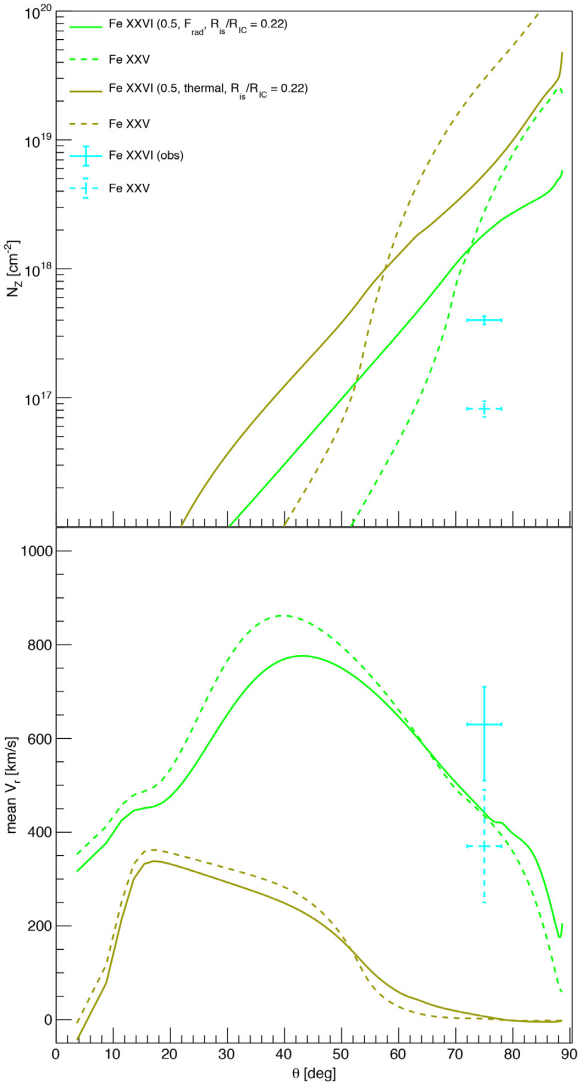

Figure 6. As in Fig. 4, but for $L = 0.5L_{\rm Ldd}$.

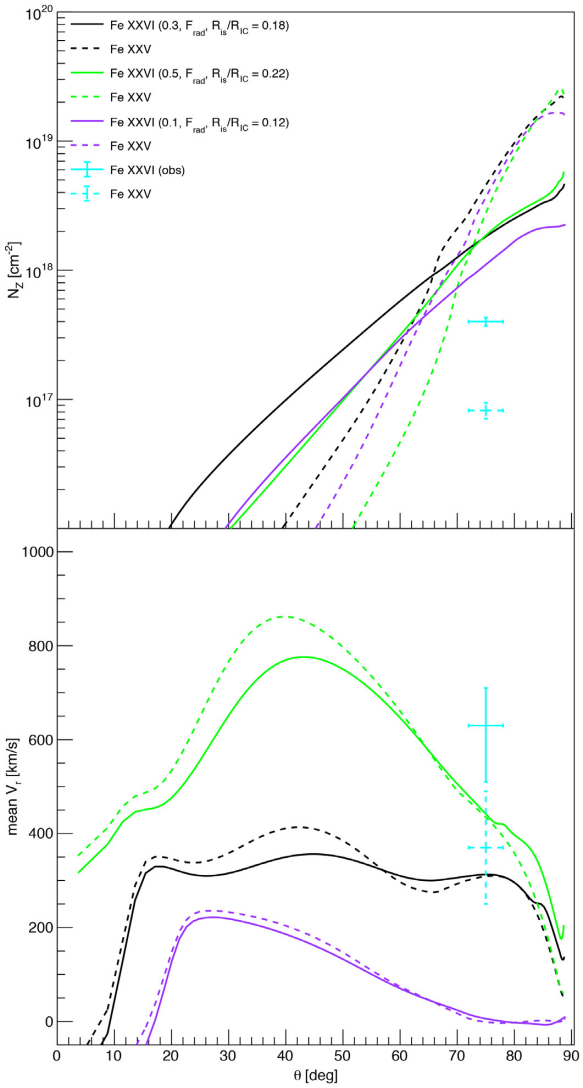

Figure 7. As in Fig. 4, but for $L/L_{\rm Edd}$ = 0.1 (violet), 0.3 (black), and 0.5 (green).

we already indicated in Section 4.2, the first is by reducing the size or height of the outer disc (the system parameters are quite uncertain, and the disc scale height need not exactly follow the irradiated disc shape; see e.g. Kimura & Done 2019), the second is by changing the irradiation pattern as a function of angle. Section 3.3 assumed a very simple exponential attenuation with angle produced by the inner corona. Density structure in the inner corona could give slightly stronger attenuation of both the disc and X-ray source at large inclination angles, or the different radiation pattern of the flat disc and more isotropic X-ray source could give different spectral illumination of the disc surface compared to that observed.

4.4 Changing the extent of the shadow from the inner attenuation zone

We quantify the ideas above by simply reduce the illumination of the outer disc by changing the shadow size to $R_{\rm is}/R_{\rm IC} = 1.0$ on each of the simulations for $L/L_{\rm Edd} = 0.3$ and 0.5, including full radiation force.

The lines in black and orange in Fig. 8 show the effect of this for $L/L_{\rm Edd} = 0.3$, while the lines in green and magenta show this for $L/L_{\rm Edd} = 0.5$. The extended shadow means that the illuminating flux is lower for the given simulation, which means that the wind mass-loss rate is lower (D18). However, the velocity remains mainly unchanged, as once the wind rises up it sees the same radiation force as before. Hence this makes the column lower, whilst maintaining the fast velocity, giving a better match to the data (cyan).

A changing radiation pattern from the flat disc and more isotropic X-ray source would have a similar effect in reducing the illumination of the disc surface, but keeping the full radiation force on the wind once it rises up, though this is more complex to model as the Compton temperature would also change as a function of height.

5 RESULT FOR THE HARD STATE SPECTRAL ENERGY DISTRIBUTION

We now consider the predicted wind properties in the hard spectral state. The yellow line in Fig. 9(a) shows the observed SED after the switch to the hard state. This has a much higher Compton temperature than the soft state (black), and the thermal equilibrium curve is now closer to the classic S curve of B83. The luminosity

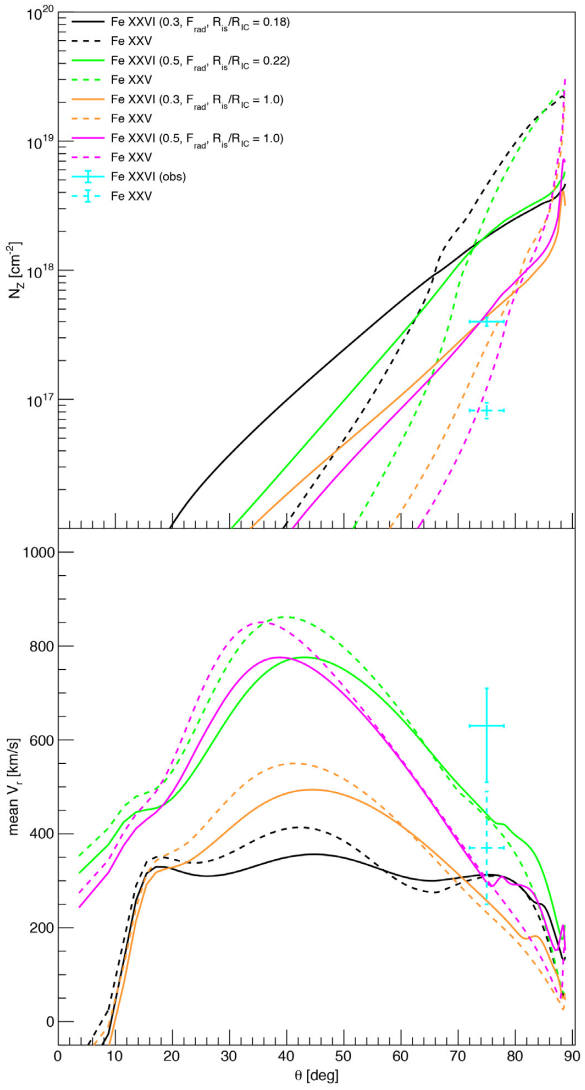

Figure 8. As in Fig. 4, but for $L/L_{\rm Edd} = 0.3$, $R_{\rm IS}/R_{\rm IC} = 0.18$ (black), $L/L_{\rm Edd} = 0.5$, $R_{\rm IS}/R_{\rm IC} = 0.22$ (green), $L/L_{\rm Edd} = 0.3$, $R_{\rm IS}/R_{\rm IC} = 1.0$ (orange), and $L/L_{\rm Edd} = 0.5$, $R_{\rm IS}/R_{\rm IC} = 1.0$ (magenta).

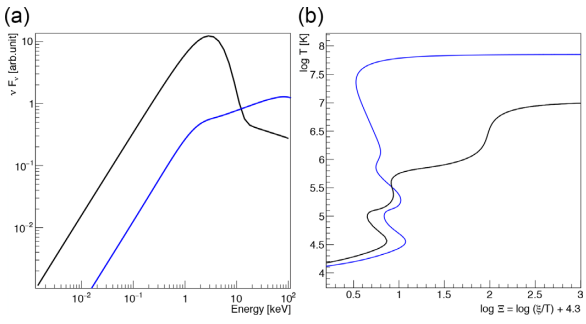

Figure 9. (a) Spectra of soft state (black) and hard state (blue). (b) The thermal equilibrium curves. Colours correspond to input spectra of (a).

is fairly low, but the high Compton temperature means that the thermal wind can be launched from closer to the black hole than in the soft state, so it can be more highly ionized (see D18). However, the key new aspect in this work is the realization that the inner attenuation zone also responds to the changing SED. The higher Compton temperature means that this has higher scale height, so it now casts a deep shadow over the entire outer disc, with $R_{\rm is} = 11R_{\rm out}$. This completely suppresses the thermal wind unless the hard X-ray source has scale height that is larger than the inner attenuation zone $H_{\rm c} \sim 20R_{\rm g}$. The response of the wind to the changing SED is not then simply due to the wind being launched from closer in, and being more highly ionized, as suggested by D18. Instead, here there is no thermal wind since the outer disc is not irradiated. The inner attenuation zone responds to the changing SED, increasing in scale height and hence increasing the shadow cast over the disc.

We run a final simulation for this hard state to confirm that the wind is suppressed sufficiently to match with the observational data. We use the hard state spectrum to calculate a new set of heating and cooling rates. These define the disc surface at $\Xi_{\rm c,max} = 12$, $T_{\rm c,max} = 3.5 \times 10^4$ K that gives the $\xi_{\rm c,max} = 22$ from thermal equilibrium curve (blue line in Fig. 9b). Thus, we set the density at the disc surface as $n = L_{\rm x}/(22R^2)$ at each time step and the grid size is same as in Section 4. We include the illumination attenuation from the inner corona but do not include line force as this is entirely negligible for highly ionized, very optically thin material.

Fig. 10 shows that the predicted iron columns are more than a factor of 10 lower than the observational upper limits (the density and temperature structure in Fig. B3), so our thermal wind simulation can indeed explain the disappearance of the wind in the hard state. This is because of overionization by the hard X-ray and large size of inner corona. In the hard state, when the thermal instability once occurs, the temperature rapidly heats up to the Compton temperature $T_{\rm IC} = 7.0 \times 10^7$ K (Fig. B3). This rapid rise gives strong gas pressure gradient force, so velocity is larger than that of soft state (Fig. 10b). The large velocity leads the low density if we consider mass continuity, also the large inner corona suppresses the wind density.

However, there is still a wind, and the mass-loss rate is over half of the mass accretion rate. We can understand this result by using the analytic estimates in D18. These show that the critical luminosity, where the Compton heating is sufficient to produce a wind from $R_{\rm IC}$, is $L_{\rm crit} \sim 0.04$. This is below the observed luminosity of $L_{\rm bol} = 0.06L_{\rm Edd}$, but the attenuation by the inner corona means that the flux illuminating the inner edge of the hydrodynamic grid is a factor of 10 lower. Thus $L/L_{\rm crit} \sim 0.1$, but the disc is large compared to $R_{\rm IC}$ ($R_{\rm out}/R_{\rm IC} = 7.0$), so the wind is still quite effective (see cyan line in fig. 3 of D18). Thermal winds have a large impact on the mass available for the outburst for systems with a large disc, explored in more detail in Dubus et al. 2019).

6 DISCUSSION

We have shown results from the first radiation hydrodynamic simulations of a thermal-radiative wind. Including the radiation force gives important differences to the structure of the thermal wind for $L > 0.1L_{\rm Edd}$ (Sections 4.1 and 4.3). We include electron scattering, bound–free absorption, and line opacity as these all give corrections that are of similar order, and all of them together act to produce a force multiplier that is large enough for these sub-Eddington flows to become super-Eddington. Thermal winds alone are too slow to match to the observed winds (see also Higginbottom et al. 2018), but these thermal-radiative winds can produce both the column density and velocity of the material seen in the soft state of H1743−322.

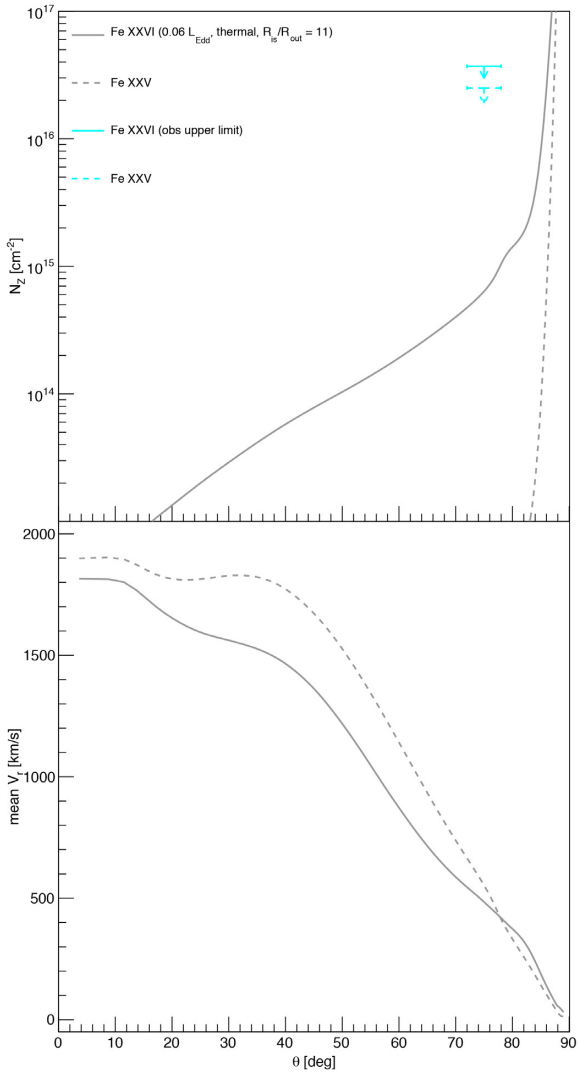

Figure 10. The angular dependence of column densities Fe XXVI (black solid line), Fe XXV (black dashed line), and those of column weighted velocities (bottom) of hard state. The cyan colours show the observational upper limit calculated from Miller et al. (2012).

We identify the key role played by the inner static corona, on size scales of a few hundred R_g (Section 4.4). This material is part of the Compton heated atmosphere of the disc, but is on size scales much less than R_{IC}, so it is bound and has $H \ll R$. None the less, it is important in determining the illumination of the outer disc where the wind arises. It is very easy for this corona to become optically thick in the equatorial plane, so that it shadows much of the outer disc from the inner disc emission. This material is below our grid scale, so we incorporate it analytically following BM83. The scale height of the inner corona casts a shadow that prevents direct illumination of the outer disc until it rises out of this shaded zone because of the intrinsically concave (saucer-like) shape of the disc. The small scale height of the inner attenuating corona in the soft state means that the outer disc is directly illuminated in the soft state. Conversely, the much larger scale height of the inner corona in the hard state completely shadows the entire disc, so the wind is suppressed. This contrasts with the explanation in D18 where the thermal wind is still present in the hard state, but is less visible due to its higher ionization that is a consequence of its smaller launch radius (Section 5). Reality may be a mixture of the two, as the structure of the hard X-ray source itself is changing during the transition. The inner disc evaporates into an X-ray hot flow whose scale height probably increases as the source dims. Evidence for this is that the electron temperature increases as shown by Motta, Muñoz-Darias & Belloni (2010), which can be modelled by an expanding hot flow region (Gardner & Done 2014; Marcel et al. 2018; Kara et al. 2019). The disc only starts further out, so the inner shadow corona starts further out, and the larger scale height of the X-rays means that some fraction can directly illuminate the outer disc as they extend above the shadow corona. A change in illumination pattern should have observable consequences on the optical continuum and on the X-ray wind properties. In bright BHB the optical continuum is generally due to reprocessing of X-rays in the outer disc, showing that the outer disc is illuminated (van Paradijs 1996). This reprocessed optical emission can be seen directly in broad-band spectra in the soft state (Hynes et al. 2002; Kimura & Done 2019), and especially in fast variability, where the optical emission is variable on time-scales of ∼1–20 s, lagged behind but correlated with the X-rays (O'Brien et al. 2002). The hard state is more complex, but close to the spectral transition there are still clear signatures that part of the optical emission is produced by reprocessing in the outer disc (Hynes et al. 2009; Veledina et al. 2017 for Swift J1753, though this reprocessing signal disappears as the source dims; Veledina et al. 2017). Simultaneous fast optical and X-ray variability data can directly measure the changing irradiation pattern on the disc and test these models of an inner attenuation zone.

The inner corona can also have an impact on the soft state spectrum. The shadow affects the corona structure when it becomes optically thick along the disc direction, but this is also associated with a vertical optical depth which is ∼0.05. Thus 5 per cent of the inner disc flux is scattered rather than being directly produced in the disc photosphere, and so at this level, it is clear that the disc emission should differ from even the best pure disc photosphere calculation such as those of Davis et al. (2005) and Davis & Hubeny (2006). This high ionization state layer on top of the disc will also change the reflected coronal flux from the disc, with around 5 per cent of the corona flux being scattered from this much higher ionization state layer than from the disc itself.

7 CONCLUSIONS

We show that thermal-radiative winds can match the observed wind properties in H1743−322. This includes both the column density and velocity of the wind seen in the soft state. We confirm the results of Higginbottom et al. (2018) that thermal winds alone are too slow, but we show that radiation pressure (on both electrons and ions) has a significant effect, producing a force multiplier that transforms these sub-Eddington luminosities to being effectively super-Eddington. Our model also shows the disappearance of the wind in the hard state due to complete shadowing of the outer disc by the inner static corona. There is no requirement for a magnetic wind to explain the behaviour of the absorption features observed in this source. We will use Monte Carlo radiation transfer to explore the detailed spectra (as in Tomaru et al. 2018) in future work.

The other black hole candidates that show absorption features from winds are likely also explained by thermal-radiative winds, especially those sources that have super-Eddington luminosities,

i.e. GRS 1915+105 and (probably) the anomalous wind seen in one observation of GRO J1655−40.

ACKNOWLEDGEMENTS

Calculation of this work is performed of the XC30 and XC50 system at the Center for Computational Astrophysics (CfCA), National Astronomical Observatory of Japan (NAOJ). This work supported by JSPS KAKENHI Grant Number JP 19J13373 (RT), Society for the Promotion of Science Grant-in-Aid for Scientific Research (A) (17H01102 KO; 16H02170 TT), Scientific Research (C) (16K05309 KO; 18K03710 KO), and Scientific Research on Innovative Areas (18H04592 KO; 18H05463 TT). This research is also supported by the Ministry of Education, Culture, Sports, Science and Technology of Japan as 'Priority Issue on Post-K computer' (Elucidation of the Fundamental Laws and Evolution of the Universe) and JICFuS. RT acknowledges the support by JSPS Overseas Challenge Program for Young Researchers. CD acknowledges the Science and Technology Facilities Council (STFC) through grant ST/P000541/1, and visitor support from Kavli IPMU.

REFERENCES

Bachiller R., 1996, ARA&A, 34, 111
Begelman M. C., McKee C. F., 1983, ApJ, 271, 89 (BM83)
Begelman M. C., McKee C. F., Shields G. A., 1983, ApJ, 271, 70 (B83)
Burrows C. J. et al., 1996, ApJ, 473, 437
Carrasco-González C., Rodríguez L. F., Anglada G., Martí J., Torrelles J. M., Osorio M., 2010, Science, 330, 1209
Coriat M., Fender R. P., Dubus G., 2012, MNRAS, 424, 1991
Cunningham C., 1976, ApJ, 208, 534
Davis S. W., Hubeny I., 2006, ApJS, 164, 530
Davis S. W., Blaes O. M., Hubeny I., Turner N. J., 2005, ApJ, 621, 372
Díaz Trigo M., Boirin L., 2016, Astron. Nachr., 337, 368
Done C., Gierliński M., Kubota A., 2007, A&AR, 15, 1
Done C., Tomaru R., Takahashi T., 2018, MNRAS, 473, 838 (D18)
Dubus G. et al., 2019, A&A, preprint (arXiv:1909.13601)
Dyda S., Dannen R., Waters T., Proga D., 2017, MNRAS, 467, 4161
Ferland G. J., 2003, ARA&A, 41, 517
Fukumura K., Kazanas D., Contopoulos I., Behar E., 2010, ApJ, 715, 636
Gardner E., Done C., 2014, MNRAS, 442, 2456
Hagino K., Odaka H., Done C., Tomaru R., Watanabe S., Takahashi T., 2016, MNRAS, 461, 3954
Harten A., 1983, J. Comput. Phys., 49, 357
Heckman T. M., Armus L., Miley G. K., 1990, ApJS, 74, 833
Higginbottom N., Proga D., 2015, ApJ, 807, 107
Higginbottom N., Knigge C., Long K. S., Matthews J. H., Sim S. A., Hewitt H. A., 2018, MNRAS, 479, 3651
Homan J., Neilsen J., Allen J. L., Chakrabarty D., Fender R., Fridriksson J. K., Remillard R. A., Schulz N., 2016, ApJ, 830, L5
Hynes R. I., Haswell C. A., Chaty S., Shrader C. R., Cui W., 2002, MNRAS, 331, 169
Hynes R. I., Brien K. O., Mullally F., Ashcraft T., 2009, MNRAS, 399, 281
Kalemci E., Begelman M. C., Maccarone T. J., Dincer T., Russell T. D., Bailyn C., Tomsick J. A., 2016, MNRAS, 463, 615
Kallman T. R., Bautista M. A., Goriely S., Mendoza C., Miller J. M., Palmeri P., Quinet P., Raymond J., 2009, ApJ, 701, 865
Kara E. et al., 2019, Nature, 565, 198
Kimura M., Done C., 2019, MNRAS, 482, 626
Luketic S., Proga D., Kallman T. R., Raymond J. C., Miller J. M., 2010, ApJ, 719, 515
Marcel G. et al., 2018, A&A, 617, A46
Miller J. M., Raymond J., Fabian A., Steeghs D., Homan J., Reynolds C. S., van der Klis M., Wijnands R., 2006a, Nature, 441, 953
Miller J. M. et al., 2006b, ApJ, 646, 394
Miller J. M. et al., 2012, ApJ, 759, L6
Miller J. M., Fabian A. C., Kaastra J., Kallman T., King A. L., Proga D., Raymond J., Reynolds C. S., 2015, ApJ, 814, 87
Mirabel I. F., Rodríguez L. F., 1999, ARA&A, 37, 409
Motta S., Muñoz-Darias T., Belloni T., 2010, MNRAS, 408, 1796
Neilsen J., Homan J., 2012, ApJ, 750, 27
Neilsen J., Lee J., 2009, Nature, 458, 481
Neilsen J., Rahoui F., Homan J., Buxton M., 2016, ApJ, 822, 20
Nomura M., Ohsuga K., Takahashi H. R., Wada K., Yoshida T., 2016, PASJ, 68, 16
O'Brien K., Horne K., Hynes R. I., Chen W., Haswell C. A., Still M. D., 2002, MNRAS, 334, 426
Ponti G., Fender R. P., Begelman M. C., Dunn R. J. H., Neilsen J., Coriat M., 2012, MNRAS, 422, L11
Ponti G., Muñoz-Darias T., Fender R. P., 2014, MNRAS, 444, 1829
Press W. H., Teukolsky S. A., Vetterling W. T., Flannery B. P., 1992, Numerical Recipes in FORTRAN. The Art of Scientific Computing, 2nd edn. Cambridge Univ. Press, Cambridge
Proga D., Kallman T. R., 2002, ApJ, 565, 455
Proga D., Kallman T. R., 2004, ApJ, 616, 688
Proga D., Stone J. M., Kallman T. R., 2000, ApJ, 543, 686
Remillard R. A., McClintock J. E., 2006, ARA&A, 44, 49
Shidatsu M., Done C., 2019, ApJ, in press (arXiv:1906.02469)
Shidatsu M., Done C., Ueda Y., 2016, ApJ, 823, 159
Steiner J. F., McClintock J. E., Reid M. J., 2012, ApJ, 745, L7
Takahashi H. R., Ohsuga K., 2013, ApJ, 772, 127
Tarter C. B., McKee C. F., 1973, ApJ, 186, L63
Tomaru R., Done C., Odaka H., Watanabe S., Takahashi T., 2018, MNRAS, 476, 1776
Tombesi F., Cappi M., Reeves J. N., Palumbo G. G. C., Yaqoob T., Braito V., Dadina M., 2010, A&A, 521, A57
Ueda Y., Yamaoka K., Remillard R., 2009, ApJ, 695, 888
Uttley P., Klein-Wolt M., 2015, MNRAS, 451, 475
van Paradijs J., 1996, ApJ, 464, L139
Veledina A., Gandhi P., Hynes R., Kajava J. J. E., Tsygankov S. S., Revnivtsev M. G., Durant M., Poutanen J., 2017, MNRAS, 470, 48
Woods D. T., Klein R. I., Castor J. I., McKee C. F., Bell J. B., 1996, ApJ, 461, 767

APPENDIX A: BASIC EQUATION AND NUMERICAL METHOD

In this section, we include for completeness the full hydrodynamic equations. We solve these in spherical polar coordinates (R, ϕ, θ).

The basic equations are the equation of continuity,

$$\frac{\partial \rho}{\partial t} + \nabla \cdot (\rho \boldsymbol{v}) = 0, \tag{A1}$$

the equation of motion,

$$\frac{\partial (\rho v_R)}{\partial t} + \nabla \cdot (\rho v_R \boldsymbol{v}) = -\frac{\partial p}{\partial R} + \rho \left(\frac{v_\theta^2}{R} + \frac{v_\phi^2}{R} + g_R + f_{\rm rad}(\xi, T) \right), \tag{A2}$$

$$\frac{\partial (\rho v_\theta)}{\partial t} + \nabla \cdot (\rho v_\theta \boldsymbol{v}) = -\frac{1}{R}\frac{\partial p}{\partial \theta} + \rho \left(-\frac{v_R v_\theta}{R} + \frac{v_\phi^2}{R} \cot\theta \right), \tag{A3}$$

$$\frac{\partial (\rho v_\phi)}{\partial t} + \nabla \cdot (\rho v_\phi \boldsymbol{v}) = -\rho \left(\frac{v_\phi v_R}{R} + \frac{v_\phi v_\theta}{R} \cot\theta \right), \tag{A4}$$

and conservation of energy,

$$\frac{\partial}{\partial t}\left[\rho\left(\frac{1}{2}v^2+e\right)\right]+\nabla\cdot\left[\rho\boldsymbol{v}\left(\frac{1}{2}v^2+e+\frac{p}{\rho}\right)\right] = \rho\boldsymbol{v}\cdot\boldsymbol{g}+\rho\mathcal{L}(\xi,T), \tag{A5}$$

where ρ is the mass density, $\boldsymbol{v}=(v_R, v_\theta, v_\phi)$ is the velocity, p is the gas pressure, e is the internal energy per unit mass, and $\boldsymbol{g}=(g_R,0)$ is the gravitational acceleration of the black hole. We assume an adiabatic equation of state $p/\rho=(\gamma-1)e$ with $\gamma=5/3$.

We set the computational domain from $R_{\rm in}=0.01R_{\rm out}\leq R\leq R_{\rm out}$, $0\leq\theta\leq\pi/2$. We solve over $N_R=120$ grid points in R and $N_\theta=240$ grid points in θ. The radial grid is set with geometric spacing as

$$R_i=R_{\rm in}(R_{\rm out}/R_{\rm in})^{i/N_R},\ (0\leq i\leq N_R). \tag{A6}$$

We set the polar angular grid in two sections, one to follow the scale height of the disc to resolve the irradiated launch region (equation 4) and one to sample the wind behaviour over the rest of the domain. We define these using the angle from the mid-plain $\alpha_j=\pi/2-\theta_{N_\theta-j}, (0\leq j\leq N_\theta)$:

$$\alpha_j=\begin{cases}\arctan\left[f_{\rm d}\left\{(R_{\rm j}/R_{\rm out})^{2/7}-(R_{\rm in}/R_{\rm out})^{2/7}\right\}\right], & (0\leq j\leq N_R),\\ \arcsin\left\{\frac{1.0-\sin(\alpha_{N_R})}{N_\theta-N_R}(j-N_R)+\sin(\alpha_{N_R})\right\}, & (N_R<j\leq N_\theta),\end{cases} \tag{A7}$$

where $\theta_0=0$, $\theta_{N_\theta}=\pi/2$. The disc surface is the top of equation (A7). At each time step, the density of disc surface is updated via $n=L_{\rm x}/(170R^2)$, where $L_{\rm x}$ is the filtered continuum.

We run CLOUDY before the hydrodynamic code, changing the ionization parameters and temperature to generate tables of net heating/cooling rate $\mathcal{L}(\xi, T)$ and force multiplier $M(\xi, T)$ in order to input into the hydrodynamic simulations. This assumes the optically thin limit, which is justified for the very highly ionized wind conditions that we are trying to reproduce here. The calculation grid of CLOUDY is a 301×121 logarithmically spaced grid (ξ, T) in a domain $1.0\times10^3\leq T\leq1.0\times10^9$ and $1.0\times10^{-3}\leq\xi\leq1.0\times10^{12}$.

The hydrodynamic terms for an ideal fluid are solved using an approximate Riemann solver, the HLL method (Harten 1983). We treat the radiation force as an explicit external force term using the force multiplier supplied via bilinear interpolation from pre-calculated CLOUDY table. The numerical procedures are (i) calculation of equations (A1)–(A4) and equation (A5) except for the net heating/cooling term, (ii) implicit update of temperature by Brent's root finding method (Press et al. 1992; see also equation A1.2 of Dyda et al. 2017) using net heating/cooling rate via bilinear interpolation from pre-calculated table by CLOUDY.

The time step is determined using the Courant–Friendrichs–Levi condition. At each grid, we calculate

$$\delta t=0.3\frac{\min(\delta R, R\delta\theta)}{\sqrt{(v_R+c_{\rm s})^2+(v_\theta+c_{\rm s})^2}}, \tag{A8}$$

where δR and $\delta\theta$ are the grid sizes, while $c_{\rm s}$ is the isothermal sound speed. The minimum value of δt in all grids is used as the time step.

APPENDIX B: DENSITY AND TEMPERATURE STRUCTURE OF ALL SIMULATIONS

We show the density and temperature structure of simulations with $L/L_{\rm LEdd}=0.3$, 0.5 (Figs B1 and B2), that of hard state (Fig. B3), and the all column densities in Table 1 (Fig. B4).

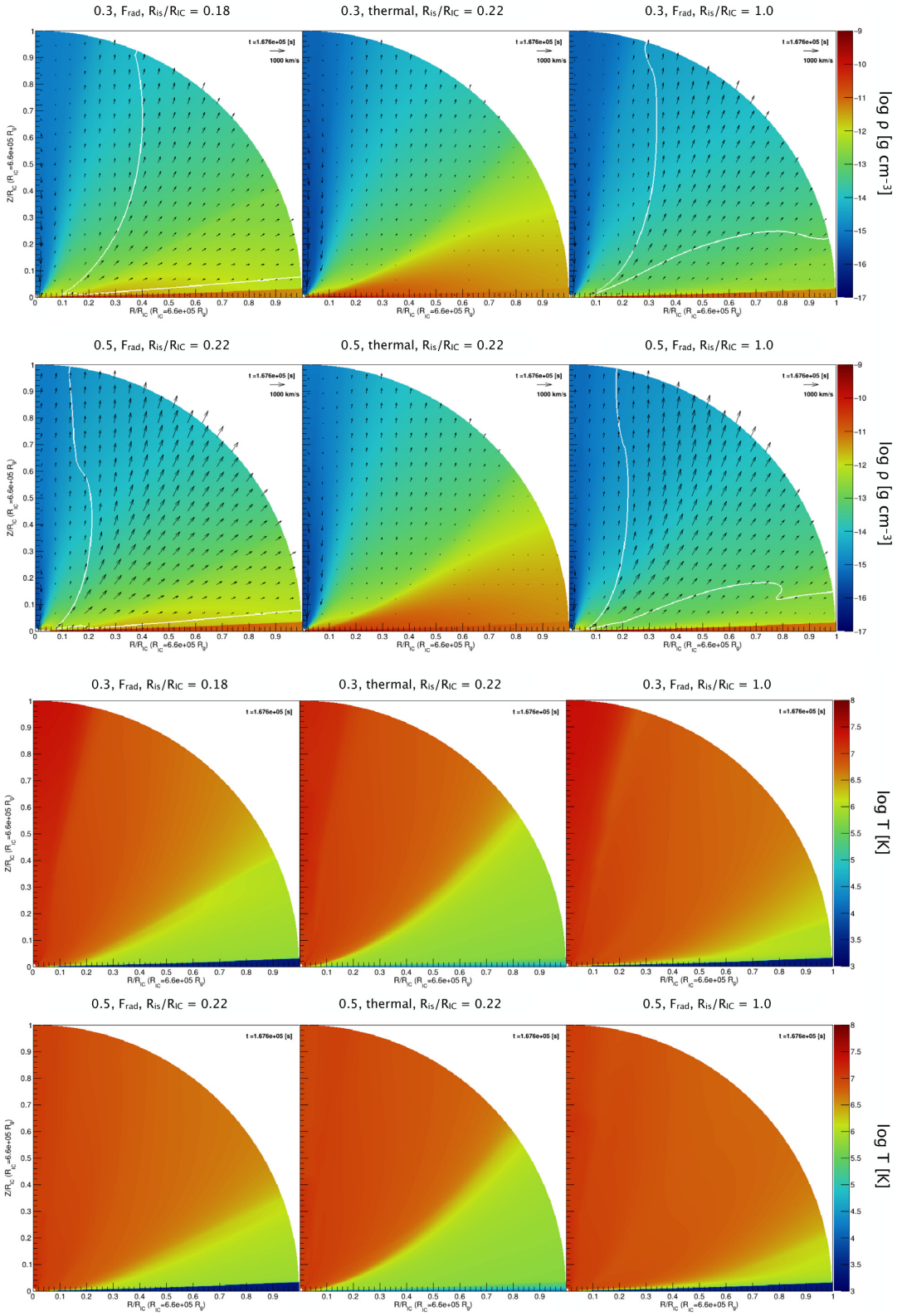

Figure B1. The density (top) and temperature (bottom) structures of final state of each simulation. Solid white lines show the Mach 1 surface of the outflow ($v_R/c_s = v_R/\sqrt{\gamma kT/(\mu m_p)} = 1$).

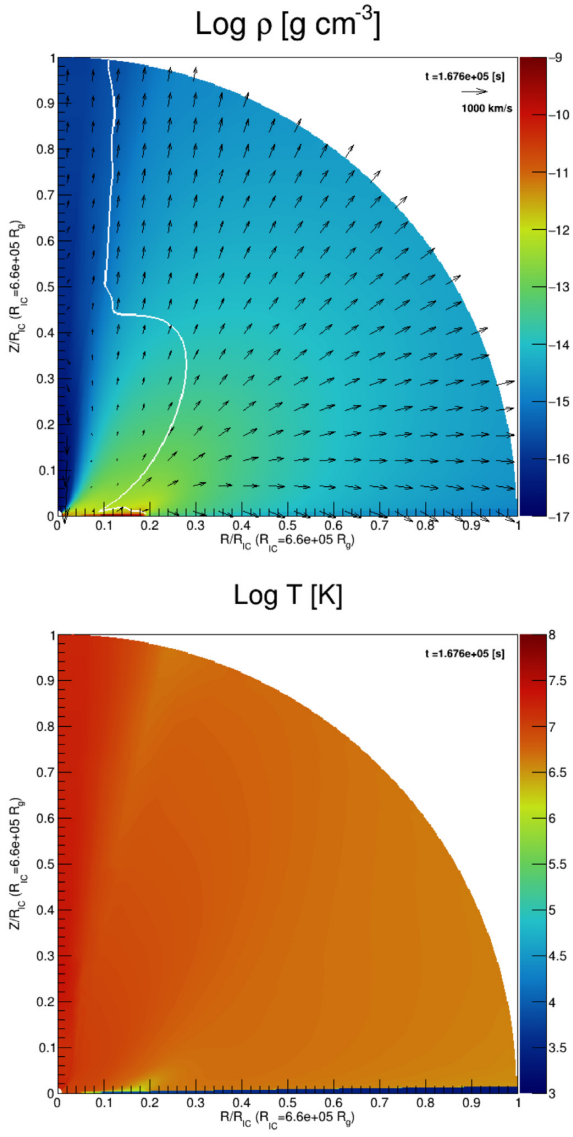

Figure B2. The density (top) and temperature (bottom) structure of small disc simulation.

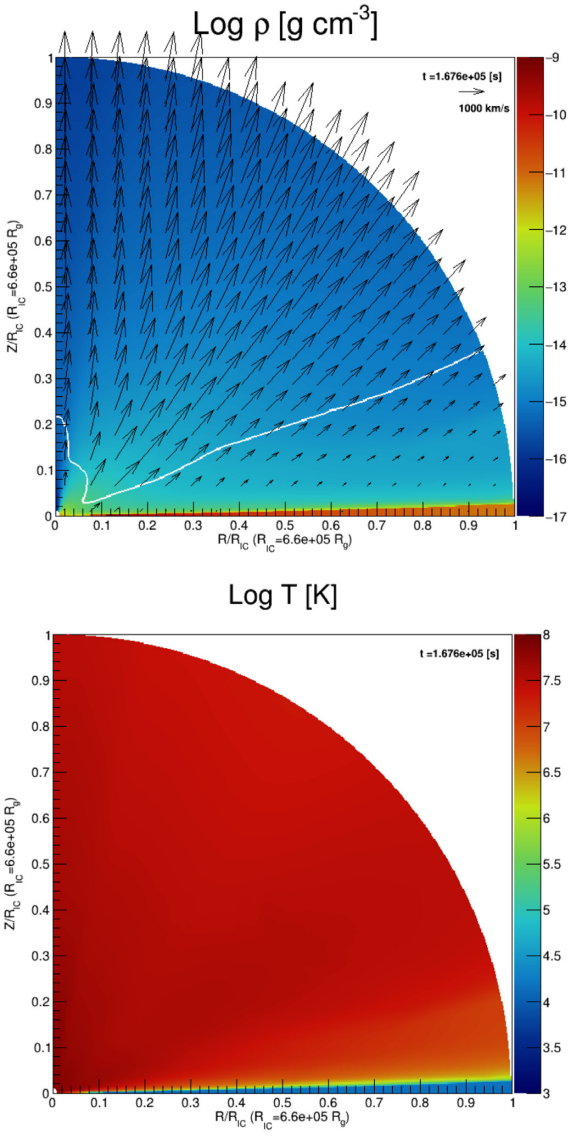

Figure B3. The density (top) and temperature (bottom) structure of hard state.

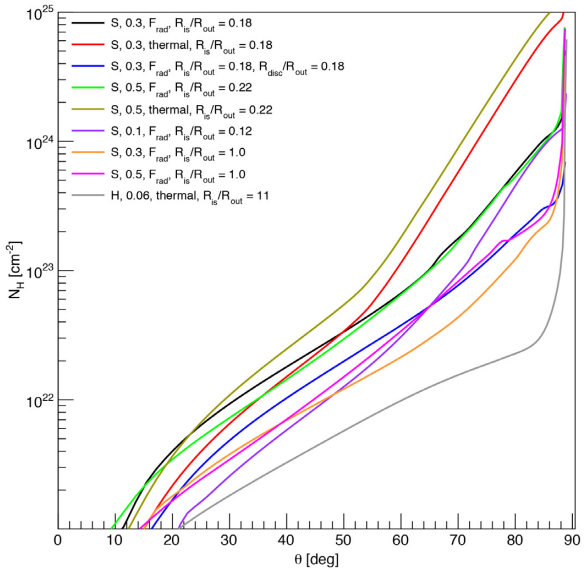

Figure B4. Hydrogen column density of all simulations in Table 1.

This paper has been typeset from a TEX/LATEX file prepared by the author.